



HAL
open science

On the significance of periglacial conditions in active mountain belts for chemical weathering processes: Insights from the Chayu area, SE Tibet

Xiaobai Ruan, Albert Galy

► **To cite this version:**

Xiaobai Ruan, Albert Galy. On the significance of periglacial conditions in active mountain belts for chemical weathering processes: Insights from the Chayu area, SE Tibet. *Chemical Geology*, 2021, 585, pp.120581. 10.1016/j.chemgeo.2021.120581 . hal-03400683

HAL Id: hal-03400683

<https://hal.science/hal-03400683>

Submitted on 5 Jan 2024

HAL is a multi-disciplinary open access archive for the deposit and dissemination of scientific research documents, whether they are published or not. The documents may come from teaching and research institutions in France or abroad, or from public or private research centers.

L'archive ouverte pluridisciplinaire **HAL**, est destinée au dépôt et à la diffusion de documents scientifiques de niveau recherche, publiés ou non, émanant des établissements d'enseignement et de recherche français ou étrangers, des laboratoires publics ou privés.



Distributed under a Creative Commons Attribution - NonCommercial 4.0 International License

1 On the significance of periglacial conditions in active mountain belts for
2 chemical weathering processes: insights from the Chayu area, SE Tibet

3
4 Xiaobai Ruan¹, Albert Galy^{1,*}

5
6 1: UL-CNRS-CRPG, 15 rue Notre Dames des Pauvres, 54500 Vandœuvre-lès-Nancy,
7 France.

8 *: corresponding author: albert.galy@univ-lorraine.fr

9
10 **Highlight**

- 11
- 12 • Periglacial conditions in active mountain belts enhance chemical weathering.
 - 13 • The weathering processes in the Chayu catchment are dominated by the
14 preferential dissolution of reactive phases such as trace carbonate and sulphide
15 and the preferential release of K from sheet silicate (biotite, chlorite).
 - 16 • In the south, under monsoonal climate, such preferential weathering can be seen
17 in bedrock landslide scars on granitoid lithology.
 - 18 • In the north, the periglacial conditions coupled with physical erosion dominated
19 by landsliding provide a strong rock exposure mechanism and the preferential
20 weathering is widespread.

21
22 **Abstract**

23
24 Chemical weathering is a key player of the long-term (Ma) timescale carbon
25 cycle. Weathering processes under alpine periglacial environment could be important
26 during the Quaternary glacial-interglacial cycles, but such timescale is difficult to
27 fully apprehend for the weathering impact on C cycles. The Chayu river catchment in
28 SE Tibet spans a geographical gradient from a periglacial environment in the north to
29 a monsoonal environment in the south and we have investigated the various chemical
30 weathering along this climatological gradient. The lithology of the catchment is
31 dominated by granitoid rocks. Due to the active tectonic activity and the periglacial
32 environment, mass wasting deposits including landslide deposits, talus and rock

33 glaciers are found in the catchment. In order to figure out the influence of mass
34 wasting process on water chemistry, we sampled seepage water from the mass
35 wasting deposits and nearby stream water for comparison. Cyclic input contributes
36 5.7 to 8.2 % to the dissolved load of the water samples, suggesting the dominance of
37 weathering contribution within this granitoid catchment. The contributions from
38 sulfuric acid and carbonate to chemical weathering are estimated based on the
39 elemental data and the oxidation of sulfide as the source of dissolved sulfate. In the
40 monsoonal South Chayu, the K^*/Si , Ca^*/Si ratios of the bedrock landslide seepages
41 are higher than the streams by 265% and 117%, respectively. Together with the high
42 contribution of carbonate (~80%) and sulfuric acid (20 to 40%), the results indicates
43 that landslide deposits have strong influences on local water chemistry by processes
44 identical to bedrock landslides of greywacke and carbonate lithology in active
45 mountain belts, suggesting that the enhanced weathering by landslide process can
46 apply to granitoid regions as well. In the North Chayu with periglacial environment,
47 the chemistry of the seepages and streams are nearly identical, and are similar to the
48 landslide seepage water in the south. Such result highlights the role of the periglacial
49 critical zone without the influence of mass wasting deposits that possibly enhances
50 chemical weathering. The high porosity created by repeat freeze-thaw cycles provides
51 more fresh mineral surfaces for water-rock interaction. But, the low temperature and
52 the partial availability of water, restricted to thaw periods, provide strong kinetic
53 limitations that inhibit the silicate weathering. Such features of the alpine periglacial
54 critical zone led to the preferential weathering of the most reactive mineral phases
55 including calcite, sulfide, and the interlayer K^+ of sheet silicates (biotite, chlorite),
56 resulting in the characteristic periglacial water chemistry. The influence of periglacial
57 environment on local water chemistry may apply beyond the North Chayu and may
58 play an important role in modulating the chemical weathering within the transition
59 between Quaternary glacial and interglacial period.

60

61 **1. Introduction**

62 The Quaternary climatic cycles may bring fluctuations of chemical weathering
63 rate and flux from regional to global scale (e.g. Colin et al., 1999; Foster and Vance,
64 2006; Hein et al., 2017; Vance et al., 2009; Wan et al., 2017; Wilson et al., 2015). As a
65 key feature of the climatic cycles, the expansion and shrinkage of ice sheet induce
66 downstream climatic impact to the broad high and middle latitudes regions (e.g.
67 Ruddiman, 2014), including the occurrence of periglacial environment over large area
68 of land surface during glacial periods (e.g. Hubberten et al., 2004; Marshall et al.,

69 2021). Periglacial environment is defined as “the climatic conditions, processes,
70 landforms, landscapes, sediments and soil structures associated with cold, nonglacial
71 environments” (Murton, 2021). The conditions of chemical weathering under
72 periglacial environment can be peculiar since repeated freeze-thaw cycles can
73 increase the porosity in bedrocks (e.g. Hallet et al., 1991; Marshall et al., 2021, 2015;
74 Sun et al., 2020) that might have played a role in the response of weathering to
75 Quaternary climate change (Foster and Vance, 2006; Vance et al., 2009).

76 Periglacial conditions are also prevailing in the cold alpine part of mountain belts,
77 and the periglacial frost cracking process is not just caused by low temperatures but
78 also by the large amplitude of diurnal or seasonal temperature variations in such
79 setting (e.g. Draebing and Krautblatter, 2019; Mair et al., 2020). This process is also
80 responsible for the ubiquitous talus deposits beneath bedrock cliffs covering valley
81 slopes (Hales and Roering, 2007), and cause high rate of physical erosion in alpine
82 mountain areas (e.g. Egholm et al., 2015; Hales and Roering, 2007). However,
83 bedrock landsliding is the dominant mass wasting process of active mountain belts
84 (Hovius et al., 2000, 1997) and the chemical weathering flux can be significantly
85 impacted by typical reactions occurring within the landslide deposits (Emberson et al.,
86 2016a). The characteristics of such chemical reactions (a strong kinetic limitation and
87 the preferential weathering of the most reactive phases) are promoted by a high
88 surface area of fresh rocks and high porosity rock mass (Emberson et al., 2018, 2017,
89 2016b). The processes of frost cracking and landsliding share the commonality of
90 breaking bedrocks and creating fresh mineral surfaces for chemical weathering.
91 Therefore, it is plausible to argue that the frost cracking under periglacial environment
92 may have strong impact on the composition of local water as well.

93 In this study, we investigated the water chemistry in the Chayu catchment in
94 Southeast Tibet, a place that spans large geographical gradient from periglacial to
95 monsoonal environment, dominated by granitoid lithology, and experiencing active
96 tectonic activity. The aim of this study is first to test the hypothesis that the mass
97 wasting deposits in periglacial environment has the effect of enhancing chemical
98 weathering and preferential weathering of labile phases, identical to the weathering of
99 bedrock landslide deposits (Emberson et al., 2018, 2017, 2016b); and second to test if
100 elevated chemical weathering in landslide deposits extends to granitoid lithologies as
101 well. By comparing the seepage waters from mass wasting deposits and the nearby
102 stream waters in two different environments in the Chayu catchment, we found (1) the
103 chemistry of both seepage and stream waters are similar and concentrated under the
104 periglacial environment, and suggestive of the preferential dissolution of calcite and

105 leaching of K from biotite coupled with sulfuric acid under periglacial environment,
106 and (2) the bedrock landslide seepages are more concentrated than streams under
107 monsoonal environment on granitoid lithology extending the characteristics of
108 bedrock landslides chemical reactions to this lithology.

109

110 **2. Study area and sampling protocol**

111 The Chayu river is the upper part of the Lohit river, an eastern tributary of the
112 Brahmaputra. It drains the eastern Himalaya for an area of ~18000 km². The
113 geography of the catchment is diverse and related to the variation in altitude. The
114 north of the catchment (North Chayu) is in a semi-arid periglacial alpine environment.
115 The surrounding mountains peak above 6000 m and the riverbed is above 3500 m. As
116 altitude decrease, the south of the catchment (South Chayu) reaches a subtropical
117 monsoonal forest environment. The lowest point of the riverbed in this area is around
118 1000 m. Near Chayu city, where the riverbed altitude is ~2000m, the mean annual
119 temperature (MAT) is 11.9° and the mean annual precipitation (MAP) is about 800
120 mm (<http://www.weather.com.cn/cityintro/101140404.shtml>). 30 km NW of North
121 Chayu, outside the catchment at 3850 m, the observed MAT is of 2.4° at the Ranwu
122 lake (Ju et al., 2017). With a mean altitude around 4600m of the North Chayu (Table
123 4), and a local thermal gradient of -6.1°/km, the MAT for North Chayu is estimated to
124 be -2.2°C. A rough estimation for MAP in the North Chayu from a satellite
125 observation-based model is less than 200 mm/yr (Anders et al., 2006).

126 Mass wasting deposits are well developed in the valley, especially in the north of
127 the catchment. Several types of mass wasting deposits can be identified based on our
128 field survey combined with satellite images (e.g. Google Earth or ArcGIS World
129 Imagery). The most prevailing type is talus (also referred to as “scree” in some
130 literature), which is the accumulation of loose rock debris, usually presented as cones,
131 at the foot of steep slopes (Ballantyne, 2002). Such landscape is frequently found in
132 alpine periglacial environment over the world (e.g. Hales and Roering, 2007 and the
133 references therein). Materials of the talus are mostly supplied by rockfall of the upper
134 rock cliffs (Ballantyne, 2002), triggered by frost cracking processes caused by the
135 stress during pore water freezing and ice segregation (e.g. Murton et al., 2006). The
136 talus deposit can experience continuous accumulation or reworking for century to
137 millennium long (e.g. Curry and Morris, 2004). Despite the temperature-related
138 processes, rock fall triggering mechanisms also include earthquakes (e.g. Matsuoka
139 and Sakai, 1999) and unloading during deglaciation (e.g. Hinchliffe and Ballantyne,
140 1999). During the Last Glacial Maximum, the high-altitude part of the Chayu valley

141 could have been covered by glacier, because the maximum extension of LGM end
142 moraines in the surrounding eastern Himalaya areas (Namcha Barwa and Parlung
143 Tsangpo Valley) are between 2800 and 3000m (Hu et al., 2020; Zhou et al., 2010).
144 However, considering the much lower MAP of the North Chayu, which means the
145 LGM glacier in North Chayu should not reach the elevation as low as the two places,
146 the newly supplied fresh rock debris on the North Chayu talus, and the intense
147 tectonic activity in the area (e.g. Mukhopadhyaya and Dasgupta, 2015), the talus
148 development in North Chayu cannot be fully ascribed to the Holocene deglaciation.
149 The second type of deposit is rock glacier, which corresponds to thick talus deposits
150 that contain permafrost and formed by the subsequent creep and deformation of such
151 rock/ice mixture (Barsch, 1992; Haeberli et al., 2006). Rock glaciers are often seen in
152 continental climate (Barsch, 1992), and favour places with high talus production rates
153 (Janke, 2007). The north part of the Chayu catchment being on the leeward slope of
154 the Mt. Kangri Garpo, it provides suitable climatic conditions for the rock glaciers. In
155 the Chayu catchment, some “talus” fans are indeed fed by the frontal collapse of rock
156 glaciers (e.g. the talus at 29°19'54.3"N, 97°5'51.0"E). The third type of deposit is
157 associated to bedrock landslide, which refers to the catastrophic movement of mass
158 bedrock along failures by gravity (Korup et al., 2007).

159 Geologically, the Chayu river catchment belongs to the eastern part of the Lhasa
160 terrane, east of the Namche Barwa Himalayan Syntaxis. The Lhasa terrane was the
161 latest geological block rifted from Gondwana, drifted northward and accreted to
162 Eurasia before its collision with the Indian continent (Zhu et al., 2011). The collision
163 with the Indian plate has been accommodated by the Tibet and Lhasa terrane through
164 strong deformation along strike-slip faults responsible for the eastern extrusion and
165 EW extension (e.g. Tapponnier, 2001). In the studied area, a dextral strike-slip fault,
166 the Jiali Fault, goes across the eastern Lhasa terrane, and the fault splits into two
167 branches in the Chayu river catchment (Fig. 1), the Parlung fault in the north and the
168 Puqu fault in the south (Lee et al., 2003). The consequences of the dextral strike-slip
169 are a N-S zonation of the lithology distribution, and similarities with the regions to the
170 west. In the Chayu river catchment, there are three basic lithological units: (1) the
171 metamorphic Precambrian basement; (2) the Mesozoic cover, and (3) the Eastern
172 Himalayan Batholith (EHB). The Precambrian basement contains an older part
173 bearing schist, leptynite, gneiss, and minor amphibolite and marble (Xu et al., 2013),
174 and a younger Neoproterozoic part made of greenschist-facies suite of clastic rocks
175 (Xie et al., 2007). The Mesozoic cover is composed of Ordovician-Devonian
176 carbonate rocks and Carboniferous-Permian slate (Dong et al., 2019). The EHB is the
177 dominant unit in the study area (Chiu et al., 2009; Dong et al., 2019; Lin et al., 2012;

178 Pan et al., 2012; Zhu et al., 2011). In the Chayu river catchment, intrusions of the
179 EHB mainly occurred in the Early Cretaceous but also in the Paleocene. The limited
180 mineralogy investigation for the EHB in the studied area show that it is constituted by
181 K-feldspar (~40%), plagioclase (~30%), quartz (~20%), biotite (~5 to 10%) and
182 accessory minerals such as hornblende, muscovite, apatite, and opaque phases (Chiu
183 et al., 2009; Lin et al., 2012). Based on the age, the location relative to the Parlung
184 and Puqu faults and the petrology, the EHB can be divided in three units, which are
185 the Demulha Batholith, the Azhagong Batholith and the Chayu Batholith along the
186 river path from north to south (Fig. 1, Lin et al., 2012). The elemental compositions of
187 these three batholiths are distinctive (Lin et al., 2012). Abundances of CaO (wt%) is
188 the highest in the Azhagong Batholith and the lowest in the Demulha Batholith and
189 anti-correlated with abundances of K₂O%. According to AFT thermochronology, this
190 area experienced strong exhumation (2.3-10 mm a⁻¹) in the Quaternary (Sun et al.,
191 2015) associated to a significant earthquake activity (e.g. Mukhopadhyaya and
192 Dasgupta, 2015). This is corroborated by the basin hypsometry that indicates intense
193 crustal shortening and uplift for the Chayu catchment (Zhang et al., 2020).

194 Field survey and sampling for the Chayu river catchment was conducted in
195 September 2019. A series of samples are collected corresponding to seepages from the
196 mass wasting deposit, bedrocks, and water and solid samples for streams nearby the
197 sampled seepages. Seepages are usually found at points where water exfiltrate from
198 the bottom of the mass wasting deposits (Table 1). For the landslide sampled in the
199 south catchment, seepages water is sourced from the scar of the landslide and flowing
200 on the surface of deposit. Some large deposits had several seepages, and we only
201 collected samples for those with high fluxes but also representative of the range of pH
202 and conductivity. Streams close the seepage sampling sites were also sampled. In the
203 south catchment, three streams near the landslide deposit (Fig. 1) correspond to small
204 (3.6 to 24 km²) catchment draining the same lithology under similar climatic
205 condition and with no evident mass wasting deposit in their upstream catchment. In
206 the north, the greater occurrence of mass wasting deposits, and the poor accessibility
207 implied that only one sampled stream (RYG 153) is without evident deposits. Streams
208 having larger upstream areas (> 100 km²) but with some deposits (RYG 114, RYG
209 126 and RYG 161) were also sampled. The locations of the seepages and stream
210 samples are shown in Fig. 1. The seepages sampled in the north catchment are mostly
211 from the Demulha Batholith, while the seepages in the south are from Chayu
212 Batholith. This study is far from being extensive since some mass wasting deposits
213 were unreachable (e.g. the bedrock landslide deposit at 28°57'45.9"N, 97°27'46.6"E,
214 on the riverside of a tributary too remote to access).

215

216 3. Methods

217 3.1 Sampling and analytical methods

218 The water samples are collected using HDPE syringe, filtered in situ through 0.2
219 μm nylon Millipore filter and stored in two HDPE bottles and one tube free of air. The
220 bottles and tube are fully rinsed with filtered sample water before using. A bottle, for
221 cations element analysis, was acidified with distilled nitric acid immediately after
222 sampling. The second bottle is for anion analysis. The conductivity, temperature, and
223 pH for the water samples are measured in situ with the thermo-hygrometer HANNA
224 9565.

225 The major elements were measured on a Thermo Scientific X-series 2 ICP-MS in
226 CRPG, using USGS M214, P62 and T223 as external standards and quality control
227 (QC). There was no systematic drift during the measurement, and the relative standard
228 deviation for all the elements are always below 10%. The Si concentration in water is
229 determined by the colorimetric method of the Mo blue complex (Mullin and Riley,
230 1955) in CRPG, with an uncertainty below 10%. The F^- , Cl^- , SO_4^{2-} and NO_3^- are
231 measured on Dionex ICS-1000 Ion Chromatograph at GFZ with USGS M214, P62,
232 M212 and M222 as QC. The uncertainty of anions is less than 10% (Emberson et al.,
233 2016b). Bicarbonate concentration is estimated by charge balance. Previous studies of
234 the dissolved chemistry of Himalayan and Southern Tibetan rivers that have measured
235 the bicarbonate by titration in the field show no systematic difference with the values
236 calculated by charge balance (e.g. Galy and France-Lanord, 1999; Hren et al., 2007).
237 The individual differences are actually within the 10% uncertainty of the
238 quantification of the others anions and cations. Therefore, the entire dataset of anions
239 and cations (Table 3) should be considered with uncertainties of 10%. The TDS is
240 calculated by summing the weight of elements of Si and all the cations, anions in per
241 unit volume.

242

243 3.2 Mapping the deposits and the stream catchments

244 The areas of the sampled mass wasting deposits are mapped through ArcGIS
245 using the detailed GPS location recorded during the field survey, and the satellite
246 image of ArcGIS World Imagery. The surface covered by fresh rocks on the deposits
247 are usually much brighter than the surface colonized by vegetation including lichen.
248 We mapped the area colonized by vegetation on each deposit and calculated the
249 vegetation coverage (Table 1). For the sampled streams, we extract their catchments

250 with the Hydrology tools in ArcGIS based on the 30-m resolution ASTER GDEM
251 (Advanced Spaceborne Thermal Emission and Reflection Radiometer Global Digital
252 Elevation Model) data (Geospatial Data Cloud, <http://www.gscloud.cn/>), and for
253 streams that is too small to be extracted, the catchments were mapped on ArcGIS by
254 hands. Then, the average altitude of the area or catchment of each deposit and stream
255 is calculated (Table 1 and 2).

256

257 **4. Results**

258 The cation, anions, silicon concentrations and TDS of the seepages and streams
259 are listed in Table 3. The pH value and water temperature are also listed, as well as the
260 altitude of the sampling sites. The data are grouped by the North Chayu and the South
261 Chayu. In the North Chayu, the seepages have a wide range of TDS, varying from 55
262 to 225 mg/L but describing a negative trend with the sampling altitude. The streams
263 have variable TDS as well but slightly lower than the seepages (49 to 173 mg/L). In
264 the South Chayu, the TDS values are generally lower than in the North Chayu, and
265 the seepages have higher TDS values (102 to 139 mg/L) than the streams (29 to 77
266 mg/L).

267 In terms of anions, the HCO_3^- is the dominant load. It makes up 71 to 95 Eq% (%
268 in equivalent units) of total anion in the north seepages, 59 to 90 Eq% in the north
269 streams, 54 to 72 Eq% in the south seepages and 70 to 76 Eq% in the south streams
270 (Fig. 2). Cl^- has concentrations between 4.4 and 14.6 $\mu\text{mol/L}$ and corresponds to a
271 minor component (<2 Eq% of total anion), suggesting that 1) no minor evaporitic
272 lithologies are present, and 2) cyclic input is very limited in the Chayu catchment.
273 SO_4^{2-} is the second most important anion, which makes up 4 to 28 Eq% of total anion
274 in the north seepages, 9 to 41 Eq% to the north streams, 19 to 36 Eq% in south
275 seepages and 11 to 12 Eq% in the south streams (Fig. 2). In terms of cations, Ca^{2+} is
276 dominant in the north streams and all the seepages (57 to 87 Eq% of total cation) but
277 appears to be lower in the south streams (52 to 69 Eq%). Na^+ shows the opposite
278 systematics, making up 13 to 23 Eq% in the south streams, which is higher than all
279 the other water samples (2 to 11 Eq%). K^+ is systematically higher in the South Chayu
280 and the highest K^+ concentration is observed in the seepages. The proportion of
281 dissolved Si in TDS span a similar range in the seepages and the streams in the north,
282 varying from 2.8 to 12.4% of TDS. The Si load in TDS is higher in the South Chayu.
283 For seepages it makes up 9.9 to 14.4% and for streams it makes up 19.6 to 37.1%. The
284 comparison between the seepages and the streams shows a greater difference in the
285 South Chayu, where the concentrations of SO_4^{2-} , Ca^{2+} and K^+ in the seepages are

286 clearly more elevated than in the streams. In the North Chayu, seepages and streams
287 are similar in composition.

288 In comparison with the rivers draining silicate lithology in (1) the Lhasa terrane
289 (e.g. Hren et al., 2007; Yu et al., 2021, Fig. 2) and (2) the southern flank of the
290 Himalaya (e.g. Galy and France-Lanord, 1999), the north Chayu seepages and streams
291 are similar with the Nyang River, in the Eastern part of the Lhasa terrane while the
292 south Chayu water samples with greater contribution of the alkalis is closer to the
293 rivers draining silicate lithologies (e.g. Lhasa River and southern Himalayan flank
294 rivers draining gneiss). However, the surface water samples from the Chayu
295 catchment have a lower Cl^- concentration and $\text{Cl}^-/\text{anions}$ ratio (Fig. 2), which is
296 different from many of the Lhasa terrane rivers impacted by hot-springs and/or
297 evaporite formations (Hren et al., 2007; Yu et al., 2021).

298

299 **5. Discussion**

300 **5.1 Cyclic input correction**

301 The rain composition (Table 4) from the network of Southeastern Tibet Stations
302 (SET, Liu et al., 2013) is used in our study to correct for the cyclic input. The closest
303 station to the Chayu valley is near Nyinchi city, about 200 km to the west to our study
304 area. Based on the low Cl^- concentrations in our samples, and the lack of correlation
305 between Cl^- and SO_4^{2-} , the weathering of evaporite lithology is unlikely. Therefore,
306 we adopt the assumption that all the dissolved chloride in surface water is from cyclic
307 input, and the correction is based on the following standard equation:

$$308 \quad [X]^* = [X]_{\text{sample}} - [X]_{\text{rain}} \times ([\text{Cl}^-]_{\text{sample}} / [\text{Cl}^-]_{\text{rain}}) \dots \dots \dots (1)$$

309 Where $[X]$ is the measured concentration of any species, and $[X]^*$ denotes the
310 concentration corrected for the cyclic input. The atmospheric contribution to our
311 samples represents 5.6 to 20.0 Eq% for Na and 0.8 to 21.5 Eq% for K, whereas Mg
312 and Ca are less impacted (0.1 to 5.2 Eq% and 1.5 to 14.5 Eq%, respectively). The
313 highest cyclic contributions are found in some seepages from the North Chayu,
314 associated with a small discharge of these seepages. More generally, the cyclic
315 contribution in the seepages is lower in the South Chayu than in the North Chayu. The
316 Chayu catchment is also poorly impacted by human activities, and this is specially the
317 case for the sampled seepages and streams. So $[X]^*$ is likely to be representative of
318 natural mineral weathering.

319

320 5.2 Source of sulphate

321 We use X_{SO_4} value to represent the proportion of sulphate in anions corrected
322 for the cyclic input, defined by the following equation:

$$323 \quad X_{\text{SO}_4} = 2 \times [\text{SO}_4^{2-}]^* / (2 \times [\text{SO}_4^{2-}]^* + [\text{HCO}_3^-]^*) \dots\dots\dots (2)$$

324 Since there is no evident evaporite unit in the lithology of the Chayu catchment
325 (Fig. 1) and given the lack of correlation between Cl^- and SO_4^{2-} , the dissolved
326 sulphate can be considered as the result of sulphide oxidation. All the X_{SO_4} values
327 are higher than 0.04 and 70% are above 0.1, suggesting the prevalence of sulphide
328 weathering in the Chayu catchment. In the Lhasa terrane, sulphide minerals are found
329 associated with Cu-bearing deposits hosted in granitoid rocks (e.g. Fu et al., 2017;
330 Hou et al., 2015), with S-bearing assemblages such as sphalerite + galena + pyrite +
331 chalcopyrite (Hou et al., 2015). However, the highest sulphate concentrations are
332 found in the streams RYG 125, RYG 126 and RYG 161. They are within a small area
333 of 300 km², with RYG 125 and 126 draining mostly pre-Cambrian metamorphic
334 sedimentary rocks, and RYG 161 draining Mesozoic sedimentary formations (Fig. 1).
335 The prevalence of sulphate in the Chayu water samples could indicate the contribution
336 of the oxidation of disseminated sulphide in the granitoids while high $[\text{SO}_4^{2-}]$ in some
337 streams are related to sedimentary lithology locally enriched in sulphide, although
338 little documented in that part of the Himalayas and Tibet but recognised ~800km to
339 the West in the Tethys Himalaya (e.g. Feng et al., 2017).

340

341 5.3 Carbonate weathering

342 The contribution of carbonate weathering (X_{carb}) can be estimated using the
343 dissolved load corrected for cyclic input (e.g. Galy and France-Lanord, 1999):

$$344 \quad X_{\text{carb}} = (2 \times \text{Ca}_{\text{carb}}^* + 2 \times \text{Mg}_{\text{carb}}^*) / (\text{Na}_{\text{riv}}^* + \text{K}_{\text{riv}}^* + 2 \times \text{Ca}_{\text{riv}}^* + 2 \times \text{Mg}_{\text{riv}}^*) \dots\dots\dots (3)$$

345 Where Na_{riv}^* , K_{riv}^* , Ca_{riv}^* and Mg_{riv}^* are measured concentrations
346 corrected for cyclic input. The $\text{Ca}_{\text{carb}}^*$ and $\text{Mg}_{\text{carb}}^*$ are calculated by subtracting
347 silicate-derived Ca and Mg from the Ca_{riv}^* and Mg_{riv}^* (Eq. (4) and Eq. (5)). This
348 assumes that there are no evaporite-derived cations in the water, likely to be the
349 case given the very low dissolved chlorine concentration (Table 3).

$$350 \quad \text{Ca}_{\text{carb}}^* = \text{Ca}_{\text{riv}}^* - \text{Ca}_{\text{sil}}^* = \text{Ca}_{\text{riv}}^* - \text{Na}^* \times (\text{Ca}/\text{Na})_{\text{sil}} \dots\dots\dots (4)$$

$$351 \quad \text{Mg}_{\text{carb}}^* = \text{Mg}_{\text{riv}}^* - \text{Mg}_{\text{sil}}^* = \text{Mg}_{\text{riv}}^* - \text{K}^* \times (\text{Mg}/\text{K})_{\text{sil}} \dots\dots\dots (5)$$

352 Of course, the $(\text{Ca}/\text{Na})_{\text{sil}}$ and $(\text{Mg}/\text{K})_{\text{sil}}$ (expressed in molar ratio) have to
353 correspond to the local composition of the silicate endmember (e.g. Galy and
354 France-Lanord, 1999). According to the mean rock composition in each unit of EHB
355 (Lin et al., 2012), the $(\text{Ca}/\text{Na})_{\text{sil}}$ for the Chayu Batholith in South Chayu and the
356 Demulha Batholith in the North Chayu are 0.277 and 0.117, respectively, and the
357 mean $(\text{Mg}/\text{K})_{\text{sil}}$ for the Chayu Batholith is 0.049. For the Demulha Batholith, the MgO
358 content is not formally listed in Lin et al. (2012), however, their limit of quantification
359 and the overall trend between MgO and SiO_2 suggest that an average MgO content of
360 0.10 ± 0.02 (weight%). Therefore, we use a $(\text{Mg}/\text{K})_{\text{sil}} = 0.023 \pm 0.007$ for the Demulha
361 Batholith. The X_{carb} is based on the bulk chemistry of the silicate endmember, and is
362 likely to only be an inaccurate estimate for the relative contribution of carbonate and
363 silicate as soon as incongruent weathering becomes important. For instance, a
364 possible incongruent release of K could be the result of the faster release of K during
365 the weathering of biotite (e.g. Chae et al., 2006; Malmström and Banwart, 1997) and
366 may significantly change the Mg/K ratio of the weathered silicate endmember. The
367 bulk $(\text{Mg}/\text{K})_{\text{sil}}$ has to be regarded as an upper limit of the $(\text{Mg}/\text{K})_{\text{sil}}$ ratios, and we also
368 consider the ratios to be 80% less according to the biotite dissolution experiments
369 (Malmström and Banwart, 1997). In this case, the $(\text{Mg}/\text{K})_{\text{sil}}$ for the Chayu Batholith
370 and Demulha Batholith used in our estimation for X_{carb} values are 0.008-0.049 and
371 0.005-0.023, respectively. Results shows that the variation of $(\text{Mg}/\text{K})_{\text{sil}}$ caused by the
372 potential incongruent release of K has little impact on the estimation of X_{carb} (Table 3).
373 A faster dissolution of Ca-bearing silicates (Ca-plagioclase or epidote, e.g. Blum and
374 Stillings 1995; Oliva et al. 2003) would correspond to an incongruent dissolution of
375 silicates and would raise the inaccuracy of the relative contribution of carbonate and
376 silicate, so only large variations in the X_{carb} can be discussed. Based on the source
377 rock $(\text{Mg}/\text{K})_{\text{sil}}$ ratios, the X_{carb} is 0.85 to 0.97 and 0.91 to 0.97 for the seepages and
378 streams in the North Chayu, respectively, and the values are 0.78 to 0.80 and 0.51 to
379 0.73 in the South Chayu, respectively. So, it is clear that (1) carbonate still contributes
380 the majority solute load (>50%) despite lithologies dominated by granitoids and (2)
381 the North Chayu water samples have higher X_{carb} values than the South Chayu.

382 All the mass wasting deposits in this study have X_{carb} values above 0.8. In pure
383 granitoid deposits and watersheds (RYG 153, 129, 114, 96, 97 and 99), disseminated
384 calcite is likely the most important carbonate source (e.g. White et al., 1999). For
385 streams partly draining sedimentary lithologies (RYG 125, 126 and 161), sedimentary
386 carbonate formations could be the dominant source.

387

388 **5.4 Comparison between the seepages and streams**

389 The influence of mass wasting deposits on chemical weathering has already been
390 recognised in the Western Southern Alps (WSA) and in Taiwan by a direct
391 comparison of the seepages from the mass wasting deposits with the nearby streams
392 (Emberson et al., 2018, 2017, 2016a). This approach allows to reduce the effects of
393 different climate and lithology, so it will be applied to the periglacial North Chayu and
394 the monsoonal South Chayu separately. In WSA and Taiwan, the differences between
395 seepages and streams are emphasised when the K^*/Si and Ca^*/Si ratios and the X_{carb}
396 and X_{SO_4} values are considered. Here, the differences of those indicators are always
397 larger in the South Chayu than in the North Chayu (Fig. 3).

398 **5.4.1 The South Chayu**

399 The X_{carb} and X_{SO_4} values and the K^*/Si and Ca^*/Si ratios are elevated in the
400 seepages. By comparison to the streams, those values are 29.5%, 350.0%, 264.6%,
401 116.7% higher in seepages, respectively.

402 In the South Chayu, the seepages are from a bedrock landslide and such contrast
403 with the nearby streams is in agreement with the studies of bedrock landslide
404 weathering from the WSA and Taiwan (Emberson et al., 2018, 2017, 2016a, 2016b)
405 although their lithologies are different from the Chayu catchment. Bedrock landslides
406 expose fresh mineral surfaces by generating landslide scar and grind the mobile rock
407 mass together with conducting water into debris and fractures (Emberson et al.,
408 2016a). Higher TDS, K^*/Si and Ca^*/Si ratios, and X_{carb} and X_{SO_4} values in seepages
409 have been associated to processes characteristic of the initiation of chemical
410 weathering with abundant fresh mineral surfaces and fluid supply (Emberson et al.,
411 2017, 2016b, 2016a): the fast dissolution of disseminated calcite (White et al., 1999)
412 and sulphide (e.g. Nicholson et al., 1988; Wildaman et al., 2004) and the fast release
413 of interlayer K from biotite (Malmström and Banwart, 1997). Results in the South
414 Chayu, fitting well with previous results for bedrock landslide weathering in
415 sedimentary or metamorphic lithologies indicate that such processes are also
416 pronounced in granitoid bedrock landslides.

417 **5.4.2 The North Chayu**

418 The results from the North Chayu are in sharp contrast with the results from the
419 South Chayu. For the north seepages and streams, the K^*/Si ratios are 0.08 to 0.46
420 and 0.2 to 0.75, respectively; the Ca^*/Si ratios are 3.61 to 11.19 and 3.18 to 13.28,
421 respectively; the X_{SO_4} are 0.04 to 0.28 and 0.09 to 0.41, respectively; and the X_{carb} is
422 0.85 to 0.97 and 0.91 to 0.97, respectively (Table 3). Regarding these parameters,

423 there are two major differences between the North and South Chayu (Fig. 3): (1) the
424 differences between the seepages and streams are negligible in the North not in the
425 South, and (2) the values are high in both the North Chayu stream and seepage waters.

426 The lack of sizable difference between the seepages and the streams may indicate
427 variable weathering conditions in the mass wasting deposits in North Chayu. Given
428 the variable nature of the studied mass wasting deposits (Table 1), weathering
429 conditions might be more diverse than those of fresh bedrock landslides. Indeed, the
430 freshness of the material in talus deposit varies greatly since they can be continuously
431 supplied by new rock mass and that they could be of different age leading to variable
432 weathering rates and yields (Emberson et al., 2016a; Taylor and Blum, 1995). One
433 rough way to estimate the recent activity of a landslide and the relative age of the
434 deposits is by vegetation coverage, because the colonization of vegetation on the
435 deposit needs a stable surface (Innes, 1985). However, in North Chayu, the vegetation
436 coverage of the mass wasting deposits (Table 1) correlate neither with the K^*/Si ratios
437 ($R^2 = 0.03$, $p = 0.04$) nor the Ca^*/Si ratios ($R^2 = 0.11$, $p = 0.06$) of the corresponding
438 seepages, which suggest that the age is not responsible for the large variations in the
439 K^*/Si and Ca^*/Si ratios of the seepages in the North Chayu.

440 The negligible difference between the seepages and streams can be a statistical
441 artefact of the large range in the K^*/Si and Ca^*/Si ratios and X_{SO_4} (Fig. 3), but two
442 other possibilities should be considered. First, the streams sampled in the North
443 Chayu are significantly influenced by mass wasting deposits. The satellite image
444 shows that talus deposits are ubiquitous on both sides of the valleys for those streams,
445 and there is just one small stream (RYG 153) among those we have sampled, which
446 has no deposits. It is worth noticing that the influence of deposits is widespread for
447 the streams in North Chayu. However, the dissolved load in the streams corresponds
448 to the mixing between a pure mass wasting deposits end-member and the weathering
449 of areas without any deposits. And some streams (RYG 129, 125, 126 and 161) have
450 K^*/Si , Ca^*/Si , X_{carb} and X_{SO_4} even higher than some seepages (RYG 117, 131,
451 139-143 and 155, Tables 3). Assuming adding water coming from a pure mass
452 wasting deposit end-member in variable proportion seems to have little impact on the
453 dissolved load of the streams. Therefore, the chemical composition of the water from
454 mass wasting deposits and the water characteristic of chemical weathering in North
455 Chayu outside the landslides (vegetated slopes or meadows at the bottom of the
456 valleys) are likely to be similar.

457 Three factors have been indicated as the key factors enhancing weathering in
458 bedrock landslides deposits (Emberson et al., 2018, 2016a): the larger mineral surface

459 for water-rocks interaction, the more favourable hydrological conditions, and the
460 occurrence of fresh rocks. Our results suggest that similar conditions should be more
461 widespread in North Chayu than just restricted to landslides and mass wasting
462 deposits in order to explain the chemistry of the streams.

463 Regarding the geomorphic processes and the climate in this region, the key
464 factor to such conditions is likely to be the periglacial environment. Under periglacial
465 environment, the repeat freeze-thaw process caused by the low temperature and large
466 amplitude of diurnal and seasonal temperature change (Marshall et al., 2021)
467 increases the density of pores and fractures in bedrock (Sun et al., 2020), as well as
468 the permeability (Takarli et al., 2008), thus increasing the surface area for water-rock
469 interaction. The estimated MAT in the North Chayu is within the range (-4 to -15°C)
470 suggested to be most effective in making fractures by ice segregation growth (Walder
471 and Hallet, 1985). However, the low temperature of the periglacial environment can in
472 turn exert kinetic limitations on chemical weathering. In addition, in the North Chayu
473 the water supply is limited. Water availability is an important factor limiting the
474 efficacy of chemical weathering (Maher and Chamberlain, 2014). The fresh surfaces
475 area created by freeze-thaw cycles are not readily exposed to chemical weathering
476 since they are ice-filled for a period of time, limiting the availability of fluids (Hall et
477 al., 2012). Only during the thaw, the rock fragments are available for weathering.
478 Moreover, low temperatures reduce the silicate weathering rate but also increase
479 carbonate solubility. A change in MAT from 11.9°C to -2.2°C, for the comparison of
480 the South Chayu with the North Chayu, induces a 15% increase in the dissolved
481 carbonate, while the silicate weathering rate decreases by 63% to 90% (using the
482 apparent activation energy of 74 ± 29 kJ mol⁻¹ of West et al., 2005 and a change in K_{sp}
483 for CaCO₃ by 133%, e.g. Bufe et al., 2021). Therefore, silicate weathering in the
484 periglacial environment is likely to be limited by the low temperature while carbonate
485 weathering is slightly increased. In addition water availability is restricted to thaw
486 periods, so periglacial environment could greatly inhibit silicate weathering. But, the
487 freeze-thaw cycles are exposing fresh surfaces, enhancing the preferential weathering
488 of the most reactive phases, e.g. the disseminated calcite and pyrite, and the release of
489 K from the biotite. The importance of such weathering of reactive mineral phases is,
490 however, only relative because silicate weathering is strongly inhibited. The positive
491 correlation between the Ca*/Si ratios and the X_{SO_4} values for the North Chayu
492 streams (Fig. 4) corroborates the carbonate weathering enhanced by sulphide
493 oxidation. And the positive correlations of K*/Si and Ca*/Si ratios and X_{carb} and X_{SO_4}
494 values with TDS* in both the seepage and stream water samples from North Chayu

495 (Fig. 5) suggest the weathering of the labile phases dominate the dissolved load in the
496 North Chayu, irrespective to the relative occurrence of mass wasting deposits.

497 To sum up, we attribute the dissolved characteristics in the North Chayu to the
498 periglacial environment. The frost process creates large surfaces areas for water-rock
499 interaction, while the hydrological conditions and low temperature just favour the
500 preferential weathering of labile phases and reduce the silicate weathering rate. As a
501 result, the chemical weathering has specific characteristics: high TDS*, K*/Si and
502 Ca*/Si ratios and X_{carb} and X_{SO_4} values.

503

504 **5.5 Implication on periglacial weathering**

505 **5.5.1 Comparison with alpine weathering of granitoids**

506 The particularity of the periglacial weathering in the North Chayu can be further
507 supported by the comparison with the large dataset of granitoid watersheds (White
508 and Blum, 1995; Oliva et al., 2003; Gurumurthy et al., 2012; Wu et al., 2013; Zhang
509 et al., 2016; Sun et al., 2019). For a direct comparison, that dataset has been corrected
510 for cyclic input following the same method used for the Chayu catchment. The K*/Si
511 and Ca*/Si ratios do not correlate with MAT, where MAT has been estimated using a
512 local thermal gradient of $-6.1^\circ/\text{km}$ and the mean altitude of the corresponding
513 catchment (Fig. 6). The data span a MAT range of 0 to 30°C , and their K*/Si ratios
514 are <0.37 and Ca*/Si ratios are <2.33 . A watershed with a K*/Si of 0.66 corresponds
515 to very high $[\text{K}^+]$ of $212 \mu\text{mol/L}$ in river water, and such values are likely to witness a
516 significant contribution from fertilizer (Sun et al., 2019) and are not considered in the
517 dataset. So with these, a rough range of water compositions draining granitoid
518 lithology under most of the environmental conditions on the earth surface is defined.
519 The data from the South Chayu streams are compatible to this range (Fig. 6a, b). In
520 contrast, the North Chayu data, draining mostly granitoid lithology as well, are much
521 higher, highlighting the effect of its periglacial environment. Although the North
522 Chayu is distinctive to all the other watersheds in the world granitoid dataset, we
523 regard that the alpine periglacial environment is not rare on the Earth surface, but are
524 only rarely studied. The alpine periglacial environment should draw attention since it
525 nurtures the headwaters of most mountain rivers.

526

527 **5.5.2 Implications on continental weathering during glacial-interglacial cycles**

528 Alpine periglacial weathering may play an important role in modulating the
529 chemical weathering during the Quaternary glacial-interglacial cycles. Several

530 hypotheses have been proposed to explain the records for past continental weathering.
531 The cyclic expansion and retreat of continental ice sheet could rejuvenise the surfaces
532 affected by chemical weathering and so boost the weathering rate (Crocket et al., 2012;
533 Foster and Vance, 2006; Vance et al., 2009). The cyclic latitudinal migration of the
534 inter-tropical convergence zone and associated variation in monsoon strength could
535 drive higher interglacial chemical flux (e.g. Hein et al., 2017; Wilson et al., 2015).
536 The exposure of continental shelf could introduce additional carbonate weathering
537 flux into the ocean during glacial periods (e.g. Stoll and Schrag, 1998), and probably
538 silicate weathering flux in tropical areas (e.g. Wan et al., 2017), although there are
539 also studies suggesting stable weathering flux during the Quaternary climate cycles
540 (e.g. von Blanckenburg et al., 2015).

541 Enhanced chemical weathering under periglacial environment is likely to require
542 significant fractured bedrock allowing deep-water penetration before the freeze-thaw
543 processes take place. Indeed, the Chayu valley is within a seismic belt (e.g.
544 Mukhopadhyaya and Dasgupta, 2015) and affected by high magnitude earthquake
545 capable of triggering landslides (e.g. Coudurier-Curveuer et al., 2020; Zhao et al.
546 2021). On the other hand, in areas sculptured by ice sheet or glacial (proglacial
547 settings) fluctuations and exposed to weathering (Foster and Vance, 2006) the
548 chemical weathering rate could be limited since the bedrock surface smoothed by ice
549 motion could lack fractures. Therefore, the most remarkable increases in chemical
550 weathering rate after ice sheet rejuvenation (Foster and Vance, 2006) will take place
551 in active mountain belts where new fractures are constantly generated due to tectonic
552 activity. Temperate areas can also become a periglacial environment during the glacial
553 expansion, e.g. central Eurasia (Hubberten et al., 2004) and mid-latitude North
554 American (Marshall et al., 2021). Among those areas, the periglacial weathering
555 mechanisms should be more significant in the active mountain belts where fractures
556 exist, and less on the stable terrains. Therefore, the alpine regions in active mountain
557 belts are likely to be much more sensitive to the Quaternary climatic change through
558 periglacial weathering.

559

560 **6. Conclusion**

561 In the Chayu catchment in the eastern Himalaya draining granitoid lithology, we
562 studied the dissolved load of the seepages water from mass wasting deposits and the
563 streams water in two regions with different climatic conditions. In the water samples
564 studied, the cations are dominated by Ca^{2+} except for the South Chayu streams in
565 which Na^+ and K^+ become important and the anions are dominated by HCO_3^- . The

566 cyclic input represents 5.7 to 8.2 % of the dissolved load. The SO_4^{2-} of the water
567 samples are mainly from the oxidation of sulphide mineral in granitoid lithology, with
568 the minor contribution from sedimentary sulphide for some North Chayu streams.
569 Carbonate weathering contribute to a large part for the dissolved load despite the
570 granitoid lithology, and the carbonate contribution is more significant in the North
571 Chayu.

572 In the South Chayu with sub-tropical monsoonal environment, the seepages are
573 found to be systematically higher in TDS*, K*/Si and Ca*/Si ratios, and X_{carb} and
574 X_{SO_4} values than the nearby streams. The differences between landslide seepage and
575 stream are identical to the previous studies about landslide weathering with other
576 lithologies (e.g. greywacke or sedimentary rock enriched with carbonate), suggesting
577 the enhanced weathering by landslide process still holds in granitoid regions.

578 In the North Chayu with alpine periglacial environment, the differences between
579 the seepages and streams are negligible and the values are high. This highlights the
580 impact of the periglacial environment. The high K*/Si, Ca*/Si and X_{SO_4} values in all
581 the periglacial water samples suggest the preferential weathering of reactive mineral
582 phases, likely related to their fresh exposure by freeze-thaw cycles. Besides,
583 earthquake is likely an important parameter, promoting landslides and exposing
584 bedrocks in the area, since seismic activity is both frequent and strong around the
585 Eastern Himalayan Syntaxis (e.g. Mukhopadhyaya and Dasgupta, 2015) and the
586 Chayu catchment is in a landslide-prone area (e.g. Coudurier-Curveuer et al., 2020;
587 Zhao et al. 2021). Therefore, the freeze-thaw process coupled with a physical erosion
588 dominated by landsliding provide a strong rock exposure mechanism in alpine
589 periglacial setting of the North Chayu. The preferential weathering of the reactive
590 mineral phases is also more dominant since the partial availability of water, restricted
591 to thaw periods and low temperature favour the preferential weathering of labile
592 mineralogical phases and mineralogical sites and reduces the weathering rates of
593 silicate. Alpine periglacial weathering is important since the headwaters of most
594 mountain rivers originates from periglacial environment and granitoids are prevalent
595 among the active mountain belts. In addition, the alpine periglacial weathering in
596 active mountain belt could play an important role in modulating the chemical
597 weathering during the Quaternary glacial-interglacial cycles.

598

599 Acknowledgement

600 This work was supported by the Second Tibetan Plateau Scientific Expedition
601 and Research (STEP) program (Grant No. 2019QZKK0707). We thank Yibo Yang and
602 Chengcheng Ye for their assistance in the field, Bernhard Zimmermann and Aimeryc
603 Schumacher for their assistance in elemental analysis and Jérôme Lavé for
604 discussions on the morphology of landslides. Thanks to Niels Hovius and Christoff
605 Andermann for the access to their analytical facilities.

606

607 **Reference**

- 608 Anders, A.M., Roe, G.H., Hallet, B., Montgomery, D.R., Finnegan, N.J., Putkonen, J.,
609 2006. Spatial patterns of precipitation and topography in the Himalaya, in:
610 Tectonics, Climate, and Landscape Evolution. Geological Society of America.
611 [https://doi.org/10.1130/2006.2398\(03\)](https://doi.org/10.1130/2006.2398(03))
- 612 Ballantyne, C.K., 2002. Paraglacial geomorphology. *Quaternary Science Reviews* 21,
613 1935–2017. [https://doi.org/10.1016/S0277-3791\(02\)00005-7](https://doi.org/10.1016/S0277-3791(02)00005-7)
- 614 Barsch, D., 1992. Permafrost creep and rockglaciers. *Permafrost and Periglacial*
615 *Processes* 3, 175–188. <https://doi.org/10.1002/ppp.3430030303>
- 616 Blum, A.E., Stillings, L.L., 1995. Feldspar dissolution kinetics, in: White, A.F.,
617 Brantley, S.L. (Eds.), *Chemical Weathering Rates of Silicate Minerals*. De
618 Gruyter, pp. 291–352. <https://doi.org/10.1515/9781501509650-009>
- 619 Bufe, A., Hovius, N., Emberson, R., Rugenstein, J.K.C., Galy, A.,
620 Hassenruck-Gudipati, H.J., Chang, J.-M., 2021. Co-variation of silicate,
621 carbonate and sulfide weathering drives CO₂ release with erosion. *Nat. Geosci.*
622 14, 211–216. <https://doi.org/10.1038/s41561-021-00714-3>
- 623 Chae, G.-T., Yun, S.-T., Kwon, M.-J., Kim, Y.-S., Mayer, B., 2006. Batch dissolution
624 of granite and biotite in water: Implication for fluorine geochemistry in
625 groundwater. *Geochem. J.* 40, 95–102. <https://doi.org/10.2343/geochemj.40.95>
- 626 Chiu, H.-Y., Chung, S.-L., Wu, F.-Y., Liu, D., Liang, Y.-H., Lin, I.-J., Iizuka, Y., Xie,
627 L.-W., Wang, Y., Chu, M.-F., 2009. Zircon U–Pb and Hf isotopic constraints
628 from eastern Transhimalayan batholiths on the precollisional magmatic and
629 tectonic evolution in southern Tibet. *Tectonophysics* 477, 3–19.
630 <https://doi.org/10.1016/j.tecto.2009.02.034>
- 631 Colin, C., Turpin, L., Bertaux, J., Desprairies, A., Kissel, C., 1999. Erosional history
632 of the Himalayan and Burman ranges during the last two glacial–interglacial
633 cycles. *Earth and Planetary Science Letters* 171, 647–660.
634 [https://doi.org/10.1016/S0012-821X\(99\)00184-3](https://doi.org/10.1016/S0012-821X(99)00184-3)
- 635 Coudurier-Curveur, A., Tapponnier, P., Okal, E., Van der Woerd, J., Kali, E.,
636 Choudhury, S., Baruah, S., Etchebes, M., Karakaş, Ç., 2020. A composite rupture
637 model for the great 1950 Assam earthquake across the cusp of the East
638 Himalayan Syntaxis. *Earth and Planetary Science Letters* 531, 115928.
639 <https://doi.org/10.1016/j.epsl.2019.115928>
- 640 Crocket, K.C., Vance, D., Foster, G.L., Richards, D.A., Tranter, M., 2012. Continental
641 weathering fluxes during the last glacial/interglacial cycle: insights from the
642 marine sedimentary Pb isotope record at Orphan Knoll, NW Atlantic. *Quaternary*
643 *Science Reviews* 38, 89–99. <https://doi.org/10.1016/j.quascirev.2012.02.004>

- 644 Curry, A.M., Morris, C.J., 2004. Lateglacial and Holocene talus slope development
645 and rockwall retreat on Mynydd Du, UK. *Geomorphology* 58, 85–106.
646 [https://doi.org/10.1016/S0169-555X\(03\)00226-5](https://doi.org/10.1016/S0169-555X(03)00226-5)
- 647 Dong, X., Peng, T., Fan, W., Zhao, G., Zhang, J., Liu, B., Gao, J., Peng, B., Liang, X.,
648 Zeng, W., Chen, L., 2019. Origin and tectonic implications of Early Cretaceous
649 high- and low-Mg series rocks and mafic enclaves in the Bomi–Chayu Fold Belt,
650 SE Tibet. *Lithos* 334–335, 102–116. <https://doi.org/10.1016/j.lithos.2019.03.018>
- 651 Draebing, D., Krautblatter, M., 2019. The Efficacy of Frost Weathering Processes in
652 Alpine Rockwalls. *Geophysical Research Letters* 46, 6516–6524.
653 <https://doi.org/10.1029/2019GL081981>
- 654 Egholm, D.L., Andersen, J.L., Knudsen, M.F., Jansen, J.D., Nielsen, S.B., 2015. The
655 periglacial engine of mountain erosion – Part 2: Modelling large-scale landscape
656 evolution. *Earth Surf. Dynam.* 3, 463–482.
657 <https://doi.org/10.5194/esurf-3-463-2015>
- 658 Emberson, R., Galy, A., Hovius, N., 2018. Weathering of Reactive Mineral Phases in
659 Landslides Acts as a Source of Carbon Dioxide in Mountain Belts. *Journal of*
660 *Geophysical Research: Earth Surface* 123, 2695–2713.
661 <https://doi.org/10.1029/2018JF004672>
- 662 Emberson, R., Galy, A., Hovius, N., 2017. Combined effect of carbonate and biotite
663 dissolution in landslides biases silicate weathering proxies. *Geochimica et*
664 *Cosmochimica Acta* 213, 418–434. <https://doi.org/10.1016/j.gca.2017.07.014>
- 665 Emberson, R., Hovius, N., Galy, A., Marc, O., 2016a. Chemical weathering in active
666 mountain belts controlled by stochastic bedrock landsliding. *Nature Geosci* 9,
667 42–45. <https://doi.org/10.1038/ngeo2600>
- 668 Emberson, R., Hovius, N., Galy, A., Marc, O., 2016b. Oxidation of sulfides and rapid
669 weathering in recent landslides. *Earth Surf. Dynam.* 4, 727–742.
670 <https://doi.org/10.5194/esurf-4-727-2016>
- 671 Feng, J.-L., Chen, F., Hu, H.-P., 2017. Isotopic study of the source and cycle of sulfur
672 in the Yamdrok Tso basin, Southern Tibet, China. *Applied Geochemistry* 85, 61–
673 72. <https://doi.org/10.1016/j.apgeochem.2017.09.005>
- 674 Foster, G.L., Vance, D., 2006. Negligible glacial–interglacial variation in continental
675 chemical weathering rates. *Nature* 444, 918–921.
676 <https://doi.org/10.1038/nature05365>
- 677 French, H.M., 2018. *The periglacial environment*, Fourth edition. ed. Wiley Blackwell,
678 Hoboken, NJ.
- 679 Fu, Q., Xu, B., Zheng, Y., Yang, Z., Hou, Z., Huang, K., Liu, Y., Zhang, C., Zhao, L.,
680 2017. Two episodes of mineralization in the Mengya’a deposit and implications

- 681 for the evolution and intensity of Pb–Zn–(Ag) mineralization in the Lhasa
682 terrane, Tibet. *Ore Geology Reviews* 90, 877–896.
683 <https://doi.org/10.1016/j.oregeorev.2017.01.008>
- 684 Galy, A., France-Lanord, C., 1999. Weathering processes in the Ganges–Brahmaputra
685 basin and the riverine alkalinity budget. *Chemical Geology* 159, 31–60.
686 [https://doi.org/10.1016/S0009-2541\(99\)00033-9](https://doi.org/10.1016/S0009-2541(99)00033-9)
- 687 Gurumurthy, G.P., Balakrishna, K., Riotte, J., Braun, J.-J., Audry, S., Shankar, H.N.U.,
688 Manjunatha, B.R., 2012. Controls on intense silicate weathering in a tropical
689 river, southwestern India. *Chemical Geology* 300–301, 61–69.
690 <https://doi.org/10.1016/j.chemgeo.2012.01.016>
- 691 Haeberli, W., Hallet, B., Arenson, L., Elconin, R., Humlum, O., Kääb, A., Kaufmann,
692 V., Ladanyi, B., Matsuoka, N., Springman, S., Mühll, D.V., 2006. Permafrost
693 creep and rock glacier dynamics. *Permafrost and Periglacial Processes* 17, 189–
694 214. <https://doi.org/10.1002/ppp.561>
- 695 Hales, T.C., Roering, J.J., 2007. Climatic controls on frost cracking and implications
696 for the evolution of bedrock landscapes. *J. Geophys. Res.* 112, F02033.
697 <https://doi.org/10.1029/2006JF000616>
- 698 Hall, K., Thorn, C., Sumner, P., 2012. On the persistence of ‘weathering.’
699 *Geomorphology* 149–150, 1–10. <https://doi.org/10.1016/j.geomorph.2011.12.024>
- 700 Hallet, B., Walder, J.S., Stubbs, C.W., 1991. Weathering by segregation ice growth in
701 microcracks at sustained subzero temperatures: Verification from an
702 experimental study using acoustic emissions. *Permafrost and Periglacial*
703 *Processes* 2, 283–300. <https://doi.org/10.1002/ppp.3430020404>
- 704 Hein, C.J., Galy, V., Galy, A., France-Lanord, C., Kudrass, H., Schwenk, T., 2017.
705 Post-glacial climate forcing of surface processes in the Ganges–Brahmaputra
706 river basin and implications for carbon sequestration. *Earth and Planetary*
707 *Science Letters* 478, 89–101. <https://doi.org/10.1016/j.epsl.2017.08.013>
- 708 Hinchliffe, S., Ballantyne, C.K., 1999. Talus accumulation and Rockwall retreat,
709 Trotternish, isle of Skye, Scotland. *Scottish Geographical Journal* 115, 53–70.
710 <https://doi.org/10.1080/00369229918737057>
- 711 Hou, Z., Duan, L., Lu, Y., Zheng, Y., Zhu, D., Yang, Zhiming, Yang, Zhusen, Wang,
712 B., Pei, Y., Zhao, Z., McCuaig, T.C., 2015. Lithospheric Architecture of the
713 Lhasa Terrane and Its Control on Ore Deposits in the Himalayan-Tibetan
714 Orogen*. *Economic Geology* 110, 1541–1575.
715 <https://doi.org/10.2113/econgeo.110.6.1541>

- 716 Hovius, N., Stark, C.P., Allen, P.A., 1997. Sediment flux from a mountain belt derived
717 by landslide mapping. *Geology* 25, 231–234.
718 [https://doi.org/10.1130/0091-7613\(1997\)025<0231:SFFAMB>2.3.CO;2](https://doi.org/10.1130/0091-7613(1997)025<0231:SFFAMB>2.3.CO;2)
- 719 Hovius, N., Stark, C.P., Hao-Tsu, C., Jiun-Chuan, L., 2000. Supply and Removal of
720 Sediment in a Landslide-Dominated Mountain Belt: Central Range, Taiwan. *The*
721 *Journal of Geology* 108, 73–89. <https://doi.org/10.1086/314387>
- 722 Hren, M.T., Chamberlain, C.P., Hilley, G.E., Blisniuk, P.M., Bookhagen, B., 2007.
723 Major ion chemistry of the Yarlung Tsangpo–Brahmaputra river: Chemical
724 weathering, erosion, and CO₂ consumption in the southern Tibetan plateau and
725 eastern syntaxis of the Himalaya. *Geochimica et Cosmochimica Acta* 71, 2907–
726 2935. <https://doi.org/10.1016/j.gca.2007.03.021>
- 727 Hu, G., Yi, C.-L., Liu, J.-H., Wang, P., Zhang, J.-F., Li, S.-H., Li, D., Huang, J., Wang,
728 H., Zhang, A., Shi, L., Shui, X., 2020. Glacial advances and stability of the
729 moraine dam on Mount Namcha Barwa since the Last Glacial Maximum, eastern
730 Himalayan syntaxis. *Geomorphology* 365, 107246.
731 <https://doi.org/10.1016/j.geomorph.2020.107246>
- 732 Hubberten, H.W., Andreev, A., Astakhov, V.I., Demidov, I., Dowdeswell, J.A.,
733 Henriksen, M., Hjort, C., Houmark-Nielsen, M., Jakobsson, M., Kuzmina, S.,
734 Larsen, E., Lunkka, J.P., Lyså, A., Mangerud, J., Möller, P., Saarnisto, M.,
735 Schirmer, L., Sher, A.V., Siegert, C., Siegert, M.J., Svendsen, J.I., 2004. The
736 periglacial climate and environment in northern Eurasia during the Last
737 Glaciation. *Quaternary Science Reviews, Quaternary Environments of the*
738 *Eurasian North (QUEEN)* 23, 1333–1357.
739 <https://doi.org/10.1016/j.quascirev.2003.12.012>
- 740 Innes, J.L., 1985. Lichenometry. *Progress in Physical Geography: Earth and*
741 *Environment* 9, 187–254. <https://doi.org/10.1177/030913338500900202>
- 742 Janke, J.R., 2007. Colorado Front Range Rock Glaciers: Distribution and Topographic
743 Characteristics. *Arctic, Antarctic, and Alpine Research* 39, 74–83.
744 [https://doi.org/10.1657/1523-0430\(2007\)39\[74:CFRRGD\]2.0.CO;2](https://doi.org/10.1657/1523-0430(2007)39[74:CFRRGD]2.0.CO;2)
- 745 Ju, J., Zhu, L., Wang, J., Cui, Y., Huang, L., Yang, R., Ma, Q., Luo, L., Wang, Y., 2017.
746 Estimating the contribution of glacial meltwater to Ranwu Lake, a proglacial
747 lake in SE Tibet, using observation data and stable isotopic analyses. *Environ*
748 *Earth Sci* 76, 229. <https://doi.org/10.1007/s12665-017-6544-6>
- 749 Korup, O., Clague, J.J., Hermanns, R.L., Hewitt, K., Strom, A.L., Weidinger, J.T.,
750 2007. Giant landslides, topography, and erosion. *Earth and Planetary Science*
751 *Letters* 261, 578–589. <https://doi.org/10.1016/j.epsl.2007.07.025>

- 752 Lee, H.-Y., Chung, S.-L., Wang, J.-R., Wen, D.-J., Lo, C.-H., Yang, T.F., Zhang, Y.,
753 Xie, Y., Lee, T.-Y., Wu, G., Ji, J., 2003. Miocene Jiali faulting and its
754 implications for Tibetan tectonic evolution. *Earth and Planetary Science Letters*
755 205, 185–194. [https://doi.org/10.1016/S0012-821X\(02\)01040-3](https://doi.org/10.1016/S0012-821X(02)01040-3)
- 756 Lin, I.-J., Chung, S.-L., Chu, C.-H., Lee, H.-Y., Gallet, S., Wu, G., Ji, J., Zhang, Y.,
757 2012. Geochemical and Sr–Nd isotopic characteristics of Cretaceous to
758 Paleocene granitoids and volcanic rocks, SE Tibet: Petrogenesis and tectonic
759 implications. *Journal of Asian Earth Sciences* 53, 131–150.
760 <https://doi.org/10.1016/j.jseaes.2012.03.010>
- 761 Liu, B., Kang, S., Sun, J., Zhang, Y., Xu, R., Wang, Y., Liu, Y., Cong, Z., 2013. Wet
762 precipitation chemistry at a high-altitude site (3,326 m a.s.l.) in the southeastern
763 Tibetan Plateau. *Environ Sci Pollut Res* 20, 5013–5027.
764 <https://doi.org/10.1007/s11356-012-1379-x>
- 765 Maher, K., Chamberlain, C.P., 2014. Hydrologic Regulation of Chemical Weathering
766 and the Geologic Carbon Cycle. *Science* 343, 1502–1504.
767 <https://doi.org/10.1126/science.1250770>
- 768 Mair, D., Lechmann, A., Delunel, R., Yeşilyurt, S., Tikhomirov, D., Vockenhuber, C.,
769 Christl, M., Akçar, N., Schlunegger, F., 2020. The role of frost cracking in local
770 denudation of steep Alpine rockwalls over millennia (Eiger, Switzerland). *Earth*
771 *Surface Dynamics* 8, 637–659. <https://doi.org/10.5194/esurf-8-637-2020>
- 772 Malmström, M., Banwart, S., 1997. Biotite dissolution at 25°C: The pH dependence
773 of dissolution rate and stoichiometry. *Geochimica et Cosmochimica Acta* 61,
774 2779–2799. [https://doi.org/10.1016/S0016-7037\(97\)00093-8](https://doi.org/10.1016/S0016-7037(97)00093-8)
- 775 Marshall, J.A., Roering, J.J., Bartlein, P.J., Gavin, D.G., Granger, D.E., Rempel, A.W.,
776 Praskievicz, S.J., Hales, T.C., 2015. Frost for the trees: Did climate increase
777 erosion in unglaciated landscapes during the late Pleistocene? *Science Advances*
778 1, e1500715. <https://doi.org/10.1126/sciadv.1500715>
- 779 Marshall, J.A., Roering, J.J., Rempel, A.W., Shafer, S.L., Bartlein, P.J., 2021.
780 Extensive Frost Weathering Across Unglaciated North America During the Last
781 Glacial Maximum. *Geophysical Research Letters* 48, e2020GL090305.
782 <https://doi.org/10.1029/2020GL090305>
- 783 Matsuoka, N., Sakai, H., 1999. Rockfall activity from an alpine cliff during thawing
784 periods. *Geomorphology* 28, 309–328.
785 [https://doi.org/10.1016/S0169-555X\(98\)00116-0](https://doi.org/10.1016/S0169-555X(98)00116-0)
- 786 Mukhopadhyaya, B., Dasgupta, S. 2015. Earthquake swarms near eastern Himalayan
787 Syntaxis along Jiali Fault in Tibet: A seismotectonic appraisal. *Geoscience*
788 *Frontiers* 6, 715–722. <http://dx.doi.org/10.1016/j.gsf.2014.12.009>

- 789 Mullin, J.B., Riley, J.P., 1955. The colorimetric determination of silicate with special
790 reference to sea and natural waters. *Analytica Chimica Acta* 12, 162–176.
791 [https://doi.org/10.1016/S0003-2670\(00\)87825-3](https://doi.org/10.1016/S0003-2670(00)87825-3)
- 792 Murton, J.B., 2021. What and where are periglacial landscapes? *Permafrost and*
793 *Periglacial Processes* 1–27. <https://doi.org/10.1002/ppp.2102>
- 794 Murton, J.B., Peterson, R., Ozouf, J.-C., 2006. Bedrock Fracture by Ice Segregation in
795 Cold Regions. *Science* 314, 1127–1129. <https://doi.org/10.1126/science.1132127>
- 796 Nicholson, R.V., Gillham, R.W., Reardon, E.J., 1988. Pyrite oxidation in
797 carbonate-buffered solution: 1. Experimental kinetics. *Geochimica et*
798 *Cosmochimica Acta* 52, 1077–1085.
799 [https://doi.org/10.1016/0016-7037\(88\)90262-1](https://doi.org/10.1016/0016-7037(88)90262-1)
- 800 Oliva, P., Viers, J., Dupré, B., 2003. Chemical weathering in granitic environments.
801 *Chemical Geology, Controls on Chemical Weathering* 202, 225–256.
802 <https://doi.org/10.1016/j.chemgeo.2002.08.001>
- 803 Pan, F.-B., Zhang, H.-F., Harris, N., Xu, W.-C., Guo, L., 2012. Oligocene magmatism
804 in the eastern margin of the east Himalayan syntaxis and its implication for the
805 India–Asia post-collisional process. *Lithos* 154, 181–192.
806 <https://doi.org/10.1016/j.lithos.2012.07.004>
- 807 Ruddiman, W.F., 2014. *Earth’s climate: past and future*, 3. ed. ed. Freeman, New York,
808 NY.
- 809 Stoll, H.M., Schrag, D.P., 1998. Effects of Quaternary Sea Level Cycles on Strontium
810 in Seawater. *Geochimica et Cosmochimica Acta* 62, 1107–1118.
811 [https://doi.org/10.1016/S0016-7037\(98\)00042-8](https://doi.org/10.1016/S0016-7037(98)00042-8)
- 812 Sun, D., Zhong, D., Ji, J., Tu, J., 2015. Inversion model of drainage basins’
813 tectono-thermal evolution through detrital AFT ages: A case study of Chayu
814 River in southeastern Tibet. *Chinese Journal of Geophysics* 58, 613–627.
815 <https://doi.org/10.6038/cjg20150223>
- 816 Sun, M., Wu, W., Ji, X., Wang, X., Qu, S., 2019. Silicate weathering rate and its
817 controlling factors: A study from small granitic watersheds in the Jiuhua
818 Mountains. *Chemical Geology* 504, 253–266.
819 <https://doi.org/10.1016/j.chemgeo.2018.11.019>
- 820 Sun, Y., Zhai, C., Xu, J., Cong, Y., Qin, L., Zhao, C., 2020. Characterisation and
821 evolution of the full size range of pores and fractures in rocks under freeze-thaw
822 conditions using nuclear magnetic resonance and three-dimensional X-ray
823 microscopy. *Engineering Geology* 271, 105616.
824 <https://doi.org/10.1016/j.enggeo.2020.105616>

- 825 Takarli, M., Prince, W., Siddique, R., 2008. Damage in granite under heating/cooling
826 cycles and water freeze–thaw condition. *International Journal of Rock*
827 *Mechanics and Mining Sciences* 45, 1164–1175.
828 <https://doi.org/10.1016/j.ijrmms.2008.01.002>
- 829 Tapponnier, P., 2001. Oblique Stepwise Rise and Growth of the Tibet Plateau. *Science*
830 294, 1671–1677. <https://doi.org/10.1126/science.105978>
- 831 Taylor, A., Blum, J.D., 1995. Relation between soil age and silicate weathering rates
832 determined from the chemical evolution of a glacial chronosequence. *Geology*.
- 833 Vance, D., Teagle, D.A.H., Foster, G.L., 2009. Variable Quaternary chemical
834 weathering fluxes and imbalances in marine geochemical budgets. *Nature* 458,
835 493–496. <https://doi.org/10.1038/nature07828>
- 836 von Blanckenburg, F., Bouchez, J., Ibarra, D.E., Maher, K., 2015. Stable runoff and
837 weathering fluxes into the oceans over Quaternary climate cycles. *Nature*
838 *Geoscience* 8, 538–542. <https://doi.org/10.1038/ngeo2452>
- 839 Walder, J., Hallet, B., 1985. A theoretical model of the fracture of rock during freezing.
840 *GSA Bulletin* 96, 336–346.
841 [https://doi.org/10.1130/0016-7606\(1985\)96<336:ATMOTF>2.0.CO;2](https://doi.org/10.1130/0016-7606(1985)96<336:ATMOTF>2.0.CO;2)
- 842 Wan, S., Clift, P.D., Zhao, D., Hovius, N., Munhoven, G., France-Lanord, C., Wang,
843 Y., Xiong, Z., Huang, J., Yu, Z., Zhang, J., Ma, W., Zhang, G., Li, A., Li, T., 2017.
844 Enhanced silicate weathering of tropical shelf sediments exposed during glacial
845 lowstands: A sink for atmospheric CO₂. *Geochimica et Cosmochimica Acta* 200,
846 123–144. <https://doi.org/10.1016/j.gca.2016.12.010>
- 847 West, A.J., Galy, A., Bickle, M., 2005. Tectonic and climatic controls on silicate
848 weathering. *Earth and Planetary Science Letters* 235, 211–228.
849 <https://doi.org/10.1016/j.epsl.2005.03.020>
- 850 White, A.F., Blum, A.E., 1995. Effects of climate on chemical weathering in
851 watersheds. *Geochimica et Cosmochimica Acta* 59, 1729–1747.
852 [https://doi.org/10.1016/0016-7037\(95\)00078-E](https://doi.org/10.1016/0016-7037(95)00078-E)
- 853 White, A.F., Bullen, T.D., Vivit, D.V., Schulz, M.S., Clow, D.W., 1999. The role of
854 disseminated calcite in the chemical weathering of granitoid rocks. *Geochimica*
855 *et Cosmochimica Acta* 63, 1939–1953.
856 [https://doi.org/10.1016/S0016-7037\(99\)00082-4](https://doi.org/10.1016/S0016-7037(99)00082-4)
- 857 Wildaman, R.A., Berner, R.A., Petsch, S., Bolton, E., Eckert, J.O., Mok, U., Evans, B.,
858 2004. The weathering of sedimentary organic matter as a control on
859 atmospheric O₂: I. Analysis of a black shale. *American Journal of Science* 304,
860 234–249.

- 861 Wilson, D.J., Galy, A., Piotrowski, A.M., Banakar, V.K., 2015. Quaternary climate
862 modulation of Pb isotopes in the deep Indian Ocean linked to the Himalayan
863 chemical weathering. *Earth and Planetary Science Letters* 424, 256–268.
864 <https://doi.org/10.1016/j.epsl.2015.05.014>
- 865 Wu, W., Zheng, H., Yang, J., Luo, C., Zhou, B., 2013. Chemical weathering,
866 atmospheric CO₂ consumption, and the controlling factors in a subtropical
867 metamorphic-hosted watershed. *Chemical Geology* 356, 141–150.
868 <https://doi.org/10.1016/j.chemgeo.2013.08.014>
- 869 Xie, Y., Peng, X., Qiangbazhaxi, Xiluolangjie, Cirenyangjin, 2007. Recent progress in
870 the study of the Neoproterozoic-Cambrian Bomi Group in the Bomi-Zayü area,
871 eastern Tibet, China. *Geological Bulletin of China* 26, 81–87.
- 872 Xu, W.-C., Zhang, H.-F., Harris, N., Guo, L., Pan, F.-B., Wang, S., 2013.
873 Geochronology and geochemistry of Mesoproterozoic granitoids in the Lhasa
874 terrane, south Tibet: Implications for the early evolution of Lhasa terrane.
875 *Precambrian Research* 236, 46–58.
876 <https://doi.org/10.1016/j.precamres.2013.07.016>
- 877 Yu, Z., Yan, N., Wu, G., Xu, T., Li, F., 2021. Chemical weathering in the upstream and
878 midstream reaches of the Yarlung Tsangpo basin, southern Tibetan Plateau.
879 *Chemical Geology* 559, 119906. <https://doi.org/10.1016/j.chemgeo.2020.119906>
- 880 Zhang, L., Liang, S., Yang, X., Gan, W., 2020. Landscape evolution of the Eastern
881 Himalayan Syntaxis based on basin hypsometry and modern crustal deformation.
882 *Geomorphology* 355, 107085. <https://doi.org/10.1016/j.geomorph.2020.107085>
- 883 Zhang, Q., Tao, Z., Ma, Z., Tang, W., Gao, Q., Xu, P., Lin, Y., 2016. Riverine
884 hydrochemistry and CO₂ consumption in the tropic monsoon region: a case
885 study in a granite-hosted basin, Hainan Island, China. *Environ Earth Sci* 75, 436.
886 <https://doi.org/10.1007/s12665-016-5250-0>
- 887 Zhao, B., Wang, Y., Li, W., Su, L., Lu, J., Zeng, L., Li, X., 2021. Insights into the
888 geohazards triggered by the 2017 Ms 6.9 Nyingchi earthquake in the east
889 Himalayan syntaxis, China. *Catena*, 205, 105467.
890 <https://doi.org/10.1016/j.catena.2021.105467>
- 891 Zhou, S., Wang, J., Xu, L., Wang, X., Colgan, P.M., Mickelson, D.M., 2010. Glacial
892 advances in southeastern Tibet during late Quaternary and their implications for
893 climatic changes. *Quaternary International, Climate Evolution and
894 Environmental Response on the Tibetan Plateau* 218, 58–66.
895 <https://doi.org/10.1016/j.quaint.2009.11.026>
- 896 Zhu, D.-C., Zhao, Z.-D., Niu, Y., Mo, X.-X., Chung, S.-L., Hou, Z.-Q., Wang, L.-Q.,
897 Wu, F.-Y., 2011. The Lhasa Terrane: Record of a microcontinent and its histories

898 of drift and growth. *Earth and Planetary Science Letters* 301, 241–255.
899 <https://doi.org/10.1016/j.epsl.2010.11.005>
900
901

902 1. Caption

903

904 Fig. 1. Simplified geological map indicating the sampling locations. a) The entire
905 Chayu catchment. b) zoomed-in map of the North Chayu. c) zoomed-in map of the
906 South Chayu. Geology and river system are from Tibetan Institute of Geological
907 Survey. 2007.1: 250 000 Geological Survey Report of Chayu Area / Ranwu Area
908 (<https://www.ngac.org.cn/>).

909

910 Fig. 2. Ternary plots representing the relative abundance, expressed in Eq/L, of the
911 major cation and anion of the studied Chayu water samples with the rivers draining
912 the Lhasa terrane (Hren et al., 2007; Yu et al., 2021) as a comparison. Ca^{2+} is
913 dominant and Cl^- is negligible in the samples of this study. The K^+ and Na^+ are more
914 significant in the South Chayu than in the North Chayu water samples.

915

916 Fig. 3. The K^*/Si , Ca^*/Si ratios (corrected for cyclic input), X_{SO_4} and X_{carb} values of
917 the water samples, grouped by location and nature. The vertical bars in the panel of
918 K^*/Si and Ca^*/Si indicate the corresponding composition of the batholiths, with the
919 red bar for the Demulha Batholith in the North Chayu and the green bar for the Chayu
920 Batholith in the South Chayu.

921

922 Fig. 4. Ca^*/Si ratios *versus* X_{SO_4} values for the North Chayu streams and seepages.
923 The black line represents the linear fit for the North Chayu streams with 95%
924 confidence interval presented by the grey shade. For the linear fit, the correlation
925 coefficient (R) is 0.931, and the P-value is 0.007.

926

927 Fig. 5. TDS^* *versus* a) K^*/Si ratios, b) Ca^*/Si ratios and c) X_{SO_4} values of the water
928 samples. The red lines and the pink shades represent the linear fits and the 95%
929 confidence interval, respectively, for the North Chayu streams except the sample RYG
930 114 (this stream shows a significantly lower TDS^* compared with other streams with
931 similar K^*/Si and Ca^*/Si ratios, thus is considered to be diluted by the melt water
932 from an upstream glacier). The linear fit is characterised by a correlation coefficient
933 (R) and a P-value of 0.986 and 0.002 in panel b, while those values are 0.926, and
934 0.024 in panel c.

935

936 Fig. 6. Mean annual Temperature (MAT) *versus* a) K*/Si ratio and b) Ca*/Si ratio for
937 the studied Chayu water samples and granitoid watersheds elsewhere (White and
938 Blum, 1995; Oliva et al., 2003; Gurumurthy et al., 2012; Wu et al., 2013; Zhang et al.,
939 2016; Sun et al., 2019). The colder North Chayu has higher K*/Si and Ca*/Si ratios
940 than other granitoid watersheds from literature, highlighting factors other than
941 temperature that enhance chemical weathering in this periglacial environment.
942

Table	1	Information		about	the	sampld	mass	wasting	deposits.
Sample ID	Deposit No.	Long.	Lat.	Altitude ^[1]	Relief	Type of mass wasting deposit	Surface Area	Vegetation Cover	
				m	m		km ²		
RYG 109, 110	ZL-1	97.1699	29.2948	4133	1312	Talus fan	0.779	39%	
RYG 119, 120	ZL-2	97.0376	29.3370	4944	673	Rock glacier	0.232	13%	
RYG 131	ZL-3	97.0947	29.3341	4306	247	Talus fan / rock glacier	0.199	62%	
RYG 139-142, 117	ZL-4	97.1095	29.3296	4263	310	Talus fan	0.231	29%	
RYG 143	ZL-5	97.1500	29.3273	3973	322	Talus fan	0.213	97%	
RYG 155	ZL-6	97.1104	29.3227	4284	385	Rock glacier	0.091	54%	
RYG 158	ZL-7	97.0571	29.3382	4390	225	Talus fan	0.113	85%	
RYG 147-149	ZL-8	97.1617	28.5993	2010	1220	Bedrock landslide	0.921	51%	

[1] The mean altitude of the deposit area.

Table 2 Information about the sampled streams

Sample ID	Region	Long.	Lat.	Catchment Area km ²	Mean Catchment Altitude m	Relief m	Estimated MAT °C
RYG 129	North Chayu	97.1653	29.3228	4.76	4836	1778	-3.6
RYG 153	North Chayu	97.1147	29.3219	0.122	4405	492	-1.0
RYG 114	North Chayu	97.1347	29.3318	189.1	5168	1992	-5.6
RYG 125	North Chayu	97.1892	29.3054	53.93	4927	2146	-4.2
RYG 126	North Chayu	97.1875	29.3142	141.5	4886	2159	-3.9
RYG 161	North Chayu	97.1819	29.1712	354.6	4655	2791	-2.5
RYG 96	South Chayu	97.2369	28.5960	8.35	2961	2261	7.8
RYG 97	South Chayu	97.1149	28.5807	24.0	3592	2947	4.0
RYG 99	South Chayu	97.1738	28.6018	3.59	2999	2183	7.6

Table	3	Chemical data of the water samples																
Sample ID	Type	Altitude m	pH	Temp. °C	Na ⁺ μmol/l	Mg ²⁺ μmol/l	K ⁺ μmol/l	Ca ²⁺ μmol/l	H ₄ SiO ₄ μmol/l	F ⁻ μmol/l	Cl ⁻ μmol/l	SO ₄ ²⁻ μmol/l	NO ₃ ⁻ μmol/l	HCO ₃ ⁻ μmol/l	TDS mg/L	X _{carb} ^[1]	X _{carb} ^[2]	
<i>North Catchment</i>																		
RYG 109	Seepage	3710	7.49	7.5	59.8	396.6	33.6	834.7	95.8	11.3	5.0	359.0	BQL	1823	201	0.96	0.96	
RYG 110	Seepage	3856	8.15	10.7	44.3	332.6	42.9	1024.1	90.1	7.3	6.4	239.0	BQL	2309	225	0.97	0.97	
RYG 119	Seepage	4661	7.84	2.9	31.3	22.3	16.7	297.7	78.0	1.5	6.3	48.0	BQL	584	62	0.93	0.93	
RYG 120	Seepage	4662	7.5	1.6	38.7	25.8	14.9	310.1	74.1	1.9	6.5	47.0	2.5	620	64	0.92	0.92	
RYG 131	Seepage	4216	7.3	8.4	99.1	74.7	29.4	510.4	108.2	5.0	8.7	42.0	10.0	1190	114	0.89	0.89	
RYG 139	Seepage	4149	8.05	5.8	103.2	79.9	24.7	495.9	82.3	3.3	12.1	37.0	3.4	1187	110	0.89	0.89	
RYG 140	Seepage	4149	7.07	6.7	90.2	80.9	26.4	461.7	84.7	1.8	12.3	30.0	11.9	1115	104	0.89	0.89	
RYG 141	Seepage	4149	8.26	3.8	95.6	97.9	19.8	462.9	80.5	2.0	8.5	31.0	BQL	1164	106	0.89	0.89	
RYG 117	Seepage	4143	8.24	3.8	98.7	166.2	14.1	423.0	68.4	1.9	8.1	43.0	9.8	1186	108	0.90	0.90	
RYG 142	Seepage	4147	7.85	7.1	90.7	205.3	13.4	408.3	68.0	2.0	7.8	51.0	5.3	1214	110	0.91	0.91	
RYG 143	Seepage	3857	8.19	5.5	208.4	198.1	27.8	627.8	90.4	35.0	14.6	129.0	10.0	1571	155	0.85	0.85	
RYG 155	Seepage	4137	7.55	4.2	67.0	87.8	17.7	320.7	64.1	2.0	9.7	88.0	5.9	707	76	0.90	0.90	
RYG 158	Seepage	4397	7.67	4.0	38.4	28.0	6.3	254.2	61.6	BQL	4.9	13.0	1.2	577	55	0.92	0.92	
RYG 129	Stream	3785	8.22	4.8	98.7	278.1	20.5	452.5	52.7	2.1	5.5	191.0	9.1	1182	124	0.91	0.91	
RYG 153	Stream	4127	7.8	5.4	35.0	47.2	16.1	246.5	74.1	0.9	4.4	30.0	BQL	573	58	0.91	0.91	
RYG 114	Stream	3949	7.94	10.3	32.4	60.0	19.8	217.7	24.2	5.2	5.7	52.0	BQL	493	49	0.91	0.91	
RYG 125	Stream	3581	7.38	6.5	47.7	291.8	25.4	563.9	50.6	3.8	5.3	359.0	3.4	1054	136	0.96	0.96	
RYG 126	Stream	3572	7.78	5.6	42.2	443.5	17.8	683.9	50.6	3.9	4.9	472.0	3.5	1360	173	0.97	0.97	
RYG 161	Stream	3311	8.19	8.9	73.4	400.0	23.9	584.3	50.9	3.7	12.1	352.0	5.6	1341	157	0.95	0.95	
<i>South Catchment</i>																		
RYG 147	Seepage	1957	8.3	20.2	73.0	53.8	115.1	443.0	117.1	93.1	6.2	114.0	BQL	854	102	0.80	0.81	
RYG 148	Seepage	2016	8.12	20.3	86.2	61.8	127.9	501.6	117.5	100.2	5.2	147.0	BQL	942	114	0.80	0.81	
RYG 149	Seepage	2125	9.12	24.6	88.2	78.8	193.3	576.1	208.7	119.9	5.7	283.0	43.6	856	139	0.78	0.79	
RYG 96	Stream	1886	7.86	15.2	104.6	48.5	55.7	288.4	158.1	107.6	7.0	47.0	BQL	626	77	0.73	0.74	
RYG 97	Stream	1650	7.5	15.8	52.5	11.1	13.5	82.0	104.7	26.8	4.7	14.0	BQL	192	29	0.60	0.61	
RYG 99	Stream	1787	7.62	19.2	114.0	35.0	49.2	126.7	220.0	80.1	6.4	30.0	BQL	340	57	0.51	0.52	

BQL: below quantification limit

[1] Calculated with the $(\text{Mg}/\text{K})_{\text{sil}}$ equals to the Mg/K ratio of the corresponding batholith.

[2] Calculated with the $(\text{Mg}/\text{K})_{\text{sil}}$ equals to 20% of the Mg/K ratio of the corresponding batholith.

Fig. 1

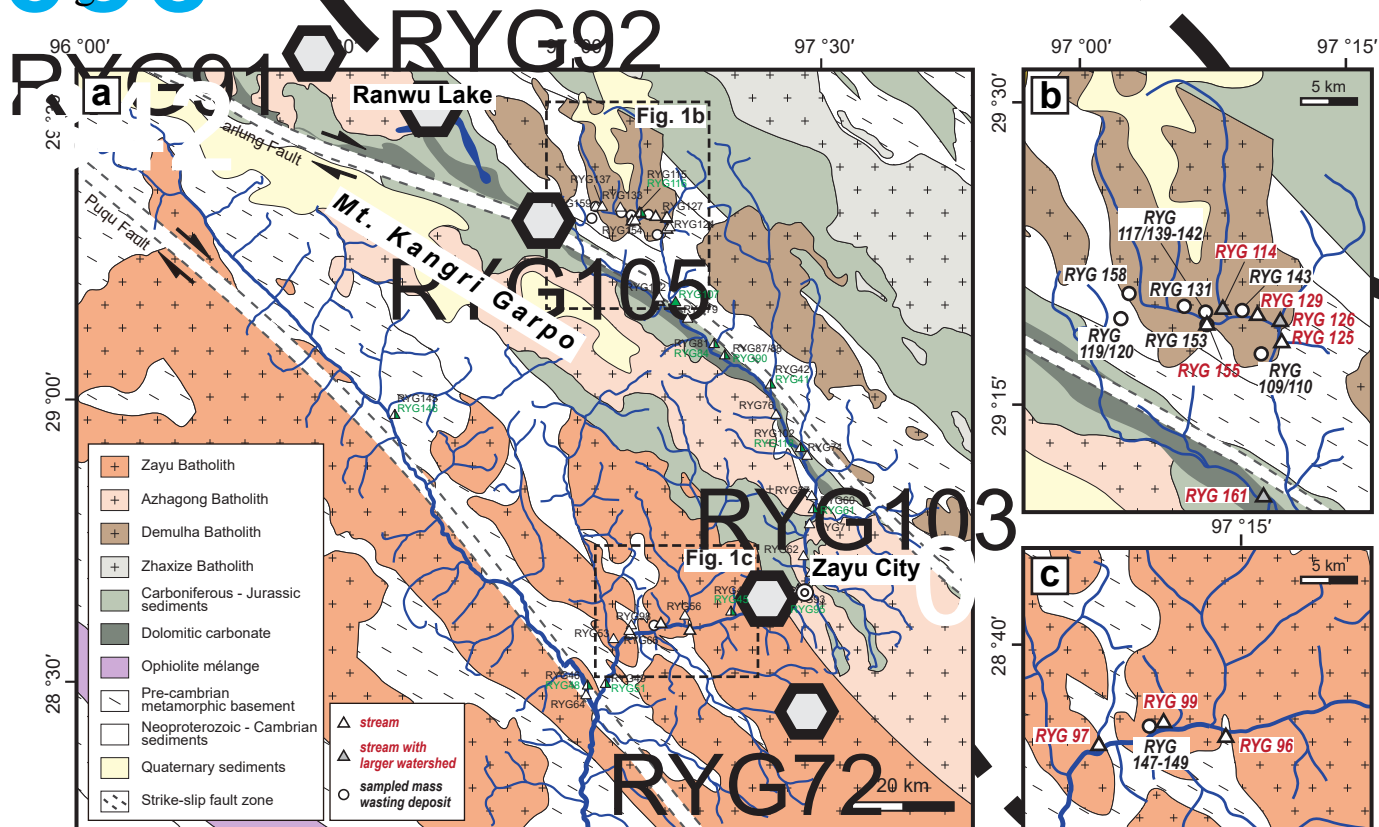


Fig. 2

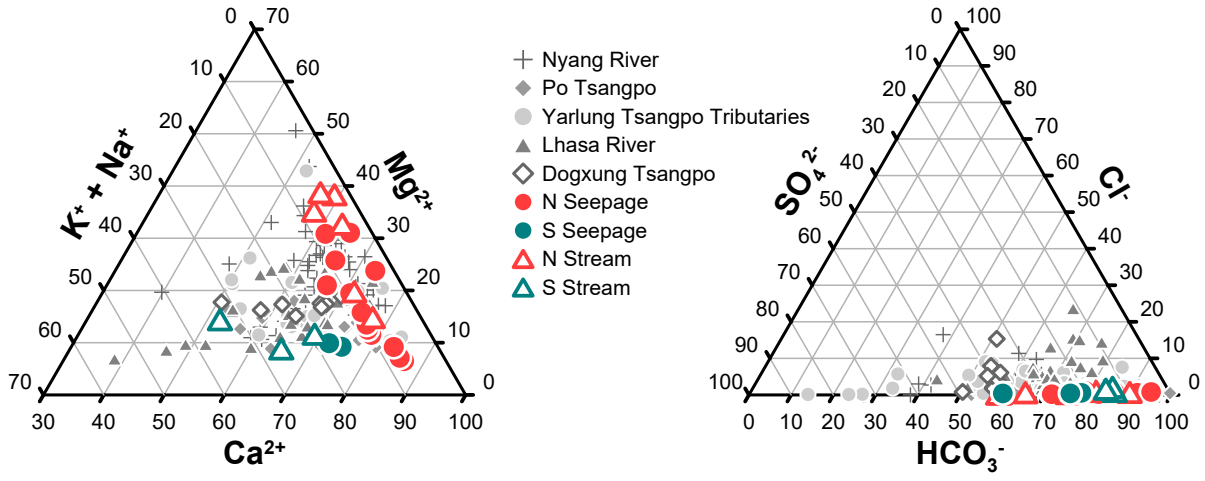


Fig. 3

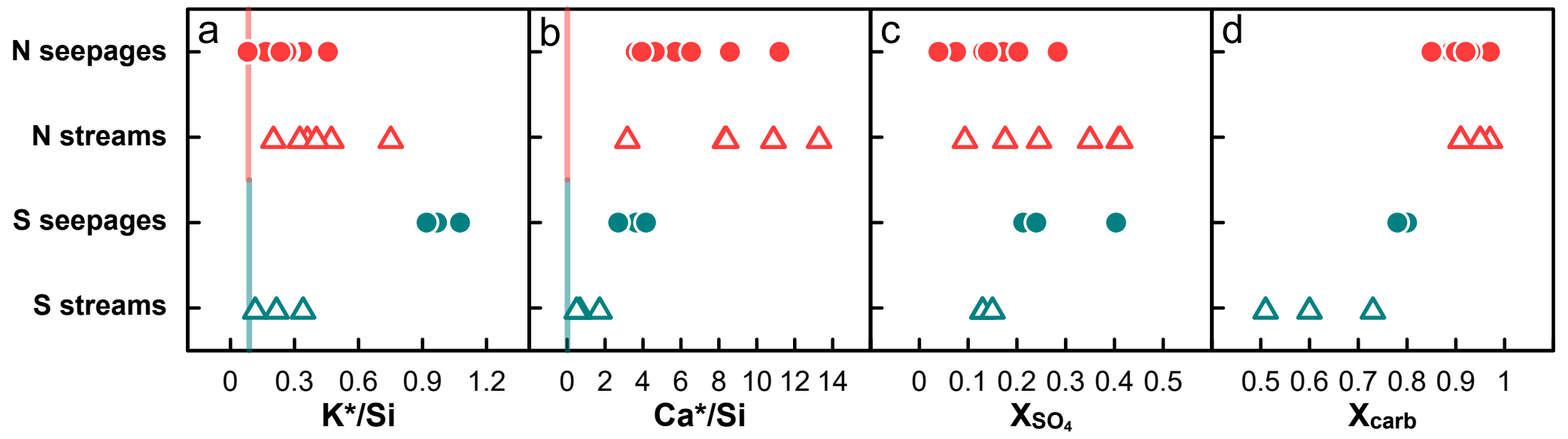


Fig. 4

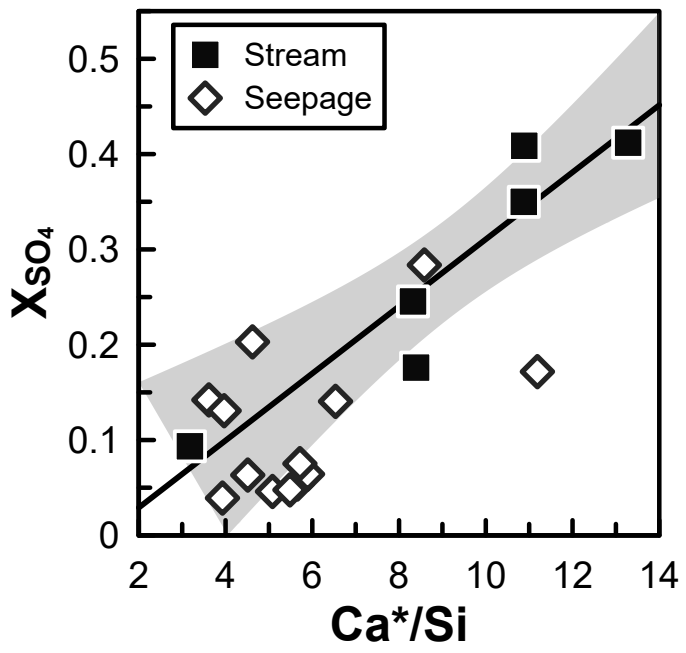


Fig. 5

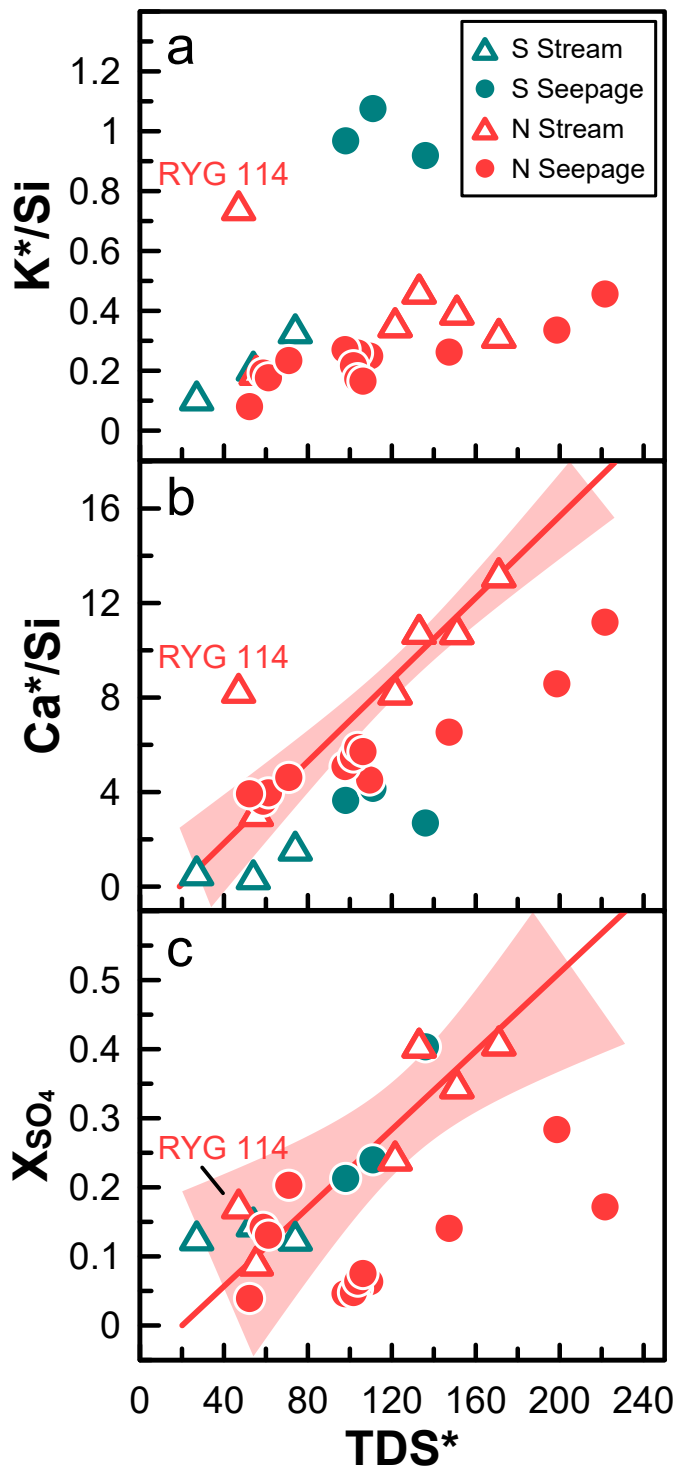


Fig. 6

